Journal of Materials Chemistry A

PAPER

View Article Online
View Journal | View Issue

Cite this: J. Mater. Chem. A, 2017, 5, 14387

Exploring the influence of iron substitution in lithium rich layered oxides $Li_2Ru_{1-x}Fe_xO_3$: triggering the anionic redox reaction†

Rohit Satish,[a] Kipil Lim,[bc] Nicolas Bucher,[d] Steffen Hartung,[d] Vanchiappan Aravindan,[e] Joseph Franklin,[efg] Jun-Sik Lee,[c] Michael F. Toney[c] and Srinivasan Madhavi*[ade]

Received 15th May 2017
Accepted 22nd June 2017

DOI: 10.1039/c7ta04194b

rsc.li/materials-a

Lithium rich layered materials are an interesting class of materials which exploit both anionic and cationic redox reactions to store energy upwards of 250 mA h g^{-1}. This paper aims to understand the nature of the redox reactions taking place in these compounds. Li_2RuO_3 was used as the base compound, which is then compared with compounds generated by partially substituting Ru with Ti and Fe respectively. Electrochemical tests indicate that Fe substitution in the sample leads to an improvement in capacity, cycle life and reduction of potential decay. To elucidate the reason for this improvement *in operando* diffraction experiments were carried out, highlighting the formation of a secondary de-lithiated phase. The distortion of the pristine structure eventually induces frontier orbital reorganization leading to the oxygen redox reaction resulting in extra capacity. Local changes at Fe and Ru ions are recorded using *in operando* X-ray absorption spectroscopy (XAS). It was noted that while Ru undergoes a reversible redox reaction, Fe undergoes a significant irreversible change in its coordination environment during cycling. The changes in the coordination environment of oxygen and formation of O_2^{n-} type species were probed *in situ* using soft X-rays.

1 Introduction

The past few years has seen an increased effort in developing high-performance cathodes for Li-ion battery applications. The main driving force behind this is to achieve high energy density batteries that can power electric vehicles over long ranges without compromising on the weight and cost of the car. Common commercially available cathodes include the layered (*e.g.* $LiCoO_2$)[1] or the 3-dimensional spinel structured (*e.g.* $LiMn_2O_4$),[2,3] or poly-anionic compounds *e.g.* olivine $LiFePO_4$ (ref. 4) which is considered a possible important potential cathode material because of its high degree of thermal stability. In the case of $LiCoO_2$ it was observed that the complete theoretical capacity of the materials cannot be exploited as the removal of more than 0.5 Li atoms from the host structure leads to permanent irreversible structural changes and capacity fade.[5–9] Substitution of cations for Co^{3+} can facilitate the minimizing of the repulsive forces between the MO_x layers thereby increasing the total capacity of the material. This led in the early 2000s to the discovery of $Li(Ni_{1/3}Mn_{1/3}Co_{1/3})O_2$ (NMC)[10] layered oxides which were noted to deliver capacities of up to 170 mA h g^{-1}, higher than both $LiMn_2O_4$ and $LiFePO_4$. Despite this positive result the material is still far from reaching its theoretical capacity of 278 mA h g^{-1}. Table 1 summarises the theoretical and practical capacity of a few commercial cathode materials in use today. Furthermore in 2006 Li-rich NMC was explored which for the first time could provide capacities exceeding 280 mA h g^{-1}.[11] But the commercialisation of these electrodes is still compromised because of issues relating to voltage fade and irreversible O_2 gas evolution above 4.5 V *vs.* Li.[12–17]

Recently materials belonging to the Li_2MO_3 (where M is 4d transition metal) family have garnered interest in the battery community because of capacities exceeding 230 mA h g^{-1}.[22] Current literature[23–26] indicates that the placement of a 4d transition metal (TM) instead of a 3d TM in $Li_2(TM)O_3$ leads to a considerable increase in cycle stability, suppression of oxygen

[a]School of Materials Science and Engineering, Nanyang Technological University, Singapore. E-mail: madhavi@ntu.edu.sg
[b]Materials Science and Engineering, Stanford University, 450 Serra Mall, Stanford, CA 94305, USA
[c]Stanford Synchrotron Radiation Lightsource, SLAC National Accelerator Laboratory, Menlo Park, CA 94025, USA
[d]TUM CREATE, Singapore 138602, Singapore
[e]Energy Research Institute @ NTU (ERI@N), Nanyang Technological University, 637553, Singapore
[f]Department of Chemical Engineering, University College London, Torrington Place, London, UK
[g]Energy Storage and Distributed Resources Division, Lawrence Berkeley National Laboratory, Berkeley, CA, 94720, USA

† Electronic supplementary information (ESI) available. See DOI: 10.1039/c7ta04194b

Table 1 List of commercial cathode materials and their theoretical and practical capacities

Composition	Theoretical capacity (mA h g^{-1})	Practical capacity (mA h g^{-1})	Reference
$LiCoO_2$	274	140	1
$LiMn_2O_4$	148	120	18
$LiFePO_4$	170	140	4
$Li(Ni_{1/3}Mn_{1/3}Co_{1/3})O_2$	278	170	10 and 19
$Li(Ni_{0.8}Co_{0.15}Al_{0.05})O_2$	279	180	20 and 21

evolution and reduction in the potential decay over time. The observed increase in capacity is attributed to the combination of cationic (TM redox) and anionic (oxygen redox) reactions.[23,27,28] The anionic redox reaction has been associated with a reversible oxo (O^{2-}) to a peroxo-like transformation (O_2^{n-}).[23] The reversible oxygen redox reaction is believed to be promoted by the metal–ligand (cation–anion band) hybridisation according to the work of Rouxel *et al.*[29,30] on layered transition metal chalcogenides and further by Tarascon *et al.*[31] in 1999.

Metal ligand covalency is a property of the materials in its ground state and it is attributed to the complex interplay between d–d coulombic interaction and the metal–ligand electronegativity difference. Initial studies based on TM–X_2 (X = S, Se and Te) exploited the use of the anionic redox reaction to store Li in the host structure and exemplary capacities were observed. As an example, TM-phosphides were observed to store up to 10 Li atoms leading to capacities exceeding 1000 mA h g^{-1},[32,33] which is in perfect agreement with the rule on ligand inductive effect, reported earlier by Goodenough *et al.*[34] But these materials exhibit a working potential of around 1.5 V *vs.* Li making their application as a cathode material not feasible. It was then hypothesized that the replacement of TM(3d) with TM(4d) or TM(5d) would lead to stronger covalent bonds between oxygen and the metal leading to higher electrochemical potentials and the involvement of the oxygen anionic redox reaction could displace the loss in capacity due to the increase in molar mass.[24]

This work focuses on the effect of substitutions on Ru based lithium rich layered compounds, Li_2RuO_3 (LRO). Ru was partially substituted with Fe (LRFO) and Ti (LRTO) in a 3 : 1 ratio, which was borrowed from previous reports by Sathiya *et al.*[23–25,35] Electrochemical studies proved that the partial substitution of Ru with Fe (LRFO), leads to an improvement in both capacity and cycle life. Similar studies have been performed by McCalla *et al.* on Li_4FeSbO_6 (ref. 36) and Li–Fe–Te oxides[37] specifically aimed at observing the oxo to peroxo transitions. Both the systems suffer from issues of high irreversible capacity loss and dramatically low cycle life. Both of the above issues are not observed when studying LRFO. The reason for the improvement in electrochemical performance was probed by using *in operando* X-ray diffraction and spectroscopic measurements. Apart from studying structural changes in the materials during cycling, we have been able to firmly establish the existence of a stable and reversible anionic redox reaction by probing the O K edge *in situ*.

2 Experimental methods

2.1 Synthesis

All the three materials were prepared using a simple solid state route according to the following chemical reaction. Where, TM is Fe or Ti.

$$Li_2CO_3 + (1 - x)RuO_2 + x(TM)O_y \rightarrow Li_2Ru_{1-x}TM_xO_3 \quad (1)$$

Li_2CO_3 (Sigma Aldrich, >99%), RuO_2 (Sigma Aldrich, 99.8% trace metal basis) Fe_2O_3 (Sigma Aldrich, 99.9%) and TiO_2 anatase (Alfa Aesar, 99%), were mixed together in stoichiometric proportions depending on the desired composition. The resulting mixture was pelletised using a 20 mm die under a force of 10 tons. The pellet was then heated at 1000 °C for 24 hours in a muffle furnace in an air atmosphere. The sintered product was removed, ground again using a mortar and pestle followed by pelletising. The resulting pellet was heated again at 900 °C for 24 hours in a muffle furnace. All the heating and cooling process' were done at a rate of 2 °C min^{-1}.

2.2 Characterisation

The resulting powders were characterised for phase purity using a Bruker D8 Advanced diffractometer arranged in a Bragg–Brentano arrangement and using a Lynxeye type detector. The obtained diffraction pattern was subjected to Rietveld refinement using TOPAS V3 software. *In operando* X-ray diffraction studies were conducted in a specialised electrochemical cell[38] designed to be used with the RIGAKU SmartLab X-ray diffractometer (200 mA, 45 kV) in reflection mode, with copper (1.54 Å) as the X-ray source. Morphological analysis was conducted using a field emission scanning electron microscope (JEOL 7600F FE-SEM).

2.3 Electrochemical cell assembly

For the purpose of electrochemical characterisation, CR2016 coin cells were assembled in a half-cell configuration with Li metal as the anode. For all half-cell studies the active material, binder (Teflonised acetylene black, TIMCAL) and conductive carbon (SuperP, TIMCAL) was mixed in a ratio of 8 : 1 : 1 (4 mg, 1 mg, 1 mg). The mixture was shaped into a pellet and pressed on a 200 mm^2 stainless steel mesh (0.25 mm thickness, Goodfellow, UK), under a force of 6 tons. The resulting electrode was dried overnight at 80 °C and 1 bar vacuum. It was then transferred into an argon filled glove-box and assembled into a coin cell.

Electrodes for the *in operando* X-ray diffraction cell were constructed in a similar fashion, but the electrode was pressed onto 20 mm diameter stainless steel mesh. The construction of the *in operando* cell is explained in detail by Hartung *et al.*[38]

Electrodes for the *in operando* X-ray absorption studies were formed by coating a mixture of the active material, PVDF and super P carbon dispersed in NMP (8 : 1 : 1) on an aluminium

foil. The coating was dried at 60 °C in ambient pressure conditions for 6 hours. The coating was cut into 12 mm diameter circles, weighed individually and dried again at 60° in 1 bar vacuum overnight. The CR2016 coin cells were modified by drilling a 3 mm hole in the centre and sealing it with Kapton tape.

Separator employed for all the tests was a porous glass fiber separator (Whatman Cat. Number: 1825-047, UK) and the electrolyte used was a 1 M solution of $LiPF_6$ dissolved in a 1 : 1 (by volume) ratio of EC (ethylene carbonate) : DEC (diethylene carbonate). Electrochemical cyclic and evaluation was conducted on a Solartron 1256E. *In operando* X-ray diffraction studies employed a BASYTECH potentiostat to cycle the coin cell. *In operando* XAS employed a Biologic SP-150 for measuring the electrochemical profile of the coin cell. Using the theoretical capacity calculations for LRO 1C was calculated to be 161 mA h g^{-1}.

2.4 X-ray absorption spectroscopy (XAS)

Ru K-edge and Fe K-edge were measured at beam line 4–1 at Stanford Synchrotron Radiation Lightsource (SSRL). The beam can operate between 5.5 keV and 38 keV with a resolution of $\Delta E/E = 10^{-4}$. It employs a Si(220) monochromator. The spectra were recorded in transmission mode in 20 minute intervals. The spectra obtained were normalised and background subtracted in order to obtain the extended X-ray absorption fine structure (EXAFS) using the ATHENA software from the Demeter Suite.[39] EXAFS analysis and fitting was carried out using ARTEMIS.[39] Reference spectra were collected for Fe and Ru and are included in Fig. S3.†

2.5 O K-edge XAS

The O K-edge XAS measurements were performed at beam line 8–2 of SSRL.[40] The XAS spectra were collected in the total electron yield (TEY) mode (penetration depth 5–10 nm) with a normal X-ray incident geometry on samples. The XAS spectra were normalized to the beam flux (I_0) measured by a gold mesh. The employed X-ray beam size was 500 μm (horizontal) × 200 μm (vertical).

3 Results and discussion

Ru based Li-rich layered cathodes (LLC) with the general formula $Li_2Ru_{0.75}M_{0.25}O_3$ (where M is Ti or Sn) have recently been the subject of multiple scientific publications because of their high capacity and high energy retention.[23–25,41] Previous results by Sathiya *et al.*[23–25,35] and Kalathil *et al.*[26] focus on the application of a d^0(Ti) and d^{10}(Sn) elements to partially substitute Ru. In this report we evaluate the effect of the partial substitution of Ru with Fe. The introduction of Fe into the system gives us a unique opportunity to observe the reversibility of the Fe(III)/Fe(IV) redox couple and its effect on the capacity and voltage properties of LLCs and also observe the reaction mechanism of the anionic oxygen redox couple which contributes to higher charge storage capacity.[23,24] It should be noted at this point that iron substitution will not lead to the exact stoichiometry of the $Li_2Ru_{0.75}M_{0.25}O_3$ instead it is expected to form a complex with oxygen vacancies allowing it to be charge balanced.

Li_2RuO_3 (LRO) and $Li_2Ru_{0.75}M_{0.25}O_3$ (where M = Ti (LRTO) or Fe (LRFO)) were synthesised using a solid state high temperature route based on earlier studies by Goodenough *et al.*[42] Low temperature (700–800 °C) sintering, leads to a lower crystallinity or a more disordered stacking structure. To improve the stacking features the sintering temperature was increased to 1000 °C and the heating and cooling rate maintained at 2 °C min^{-1}.

These materials can be considered as a solid solution of two layered structures, $LiMO_2$ and $Li_2M'O_3$ or as a single component, $Li[Li_{1/3}M_{2/3-x}M'_x]O_2$. They are composed of alternate layers of Li and LiM_2. The LiM_2 layer forms a honeycomb structure in which Li ions are surrounded by 6 TM atoms illustrated in Fig. 1. Li_2MO_3 type materials crystallise in different patterns depending on the TM. Ru, Ti and Zr[42–44] have been shown to crystallize in a monoclinic $C2/c$ space group, whereas, introduction of Mn, Sn, Ir and Rh leads to the formation of $C2/m$[45–47] and the introduction of metals like Pt[48] and Mo[49] leads to the superstructure with a rhombohedral $R3m$ structure.

X-ray diffraction data was collected for LRO, LRFO and LRTO between 15 and 50° with a step size of 0.02°. Fig. 2 indicates the diffraction pattern of LRO, LRFO and LRTO. The base structure is indexed according to JCPDS no. 84-1608 with space group $C2/c$ previously reported by Goodenough *et al.*[42] Apart from the region indicated in Fig. 2 as superstructure the rest of the peaks

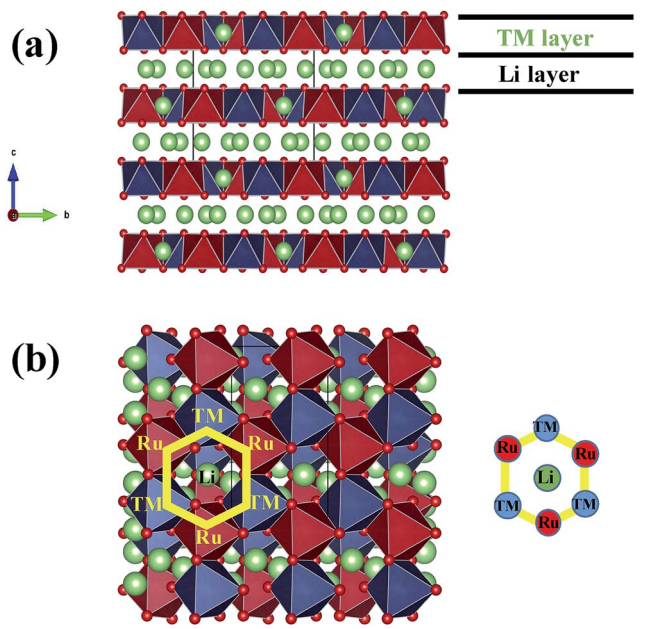

Fig. 1 Crystal structure of LLCs as viewed from the; (a) *a* axis indicating alternate layers of TM and Li layers; (b) *c* axis indicating the arrangement of Ru and substituted TM metals in a hexagonal network (yellow) around Li (TM can be Ti, Sn and Fe). The 3d TM and Ru atoms are distributed in a 1 : 1 ratio to clearly indicate the hexagonal network around Li. A more realistic visualisation would be to have 3d TM randomly occupy a quarter of the original Ru sites.

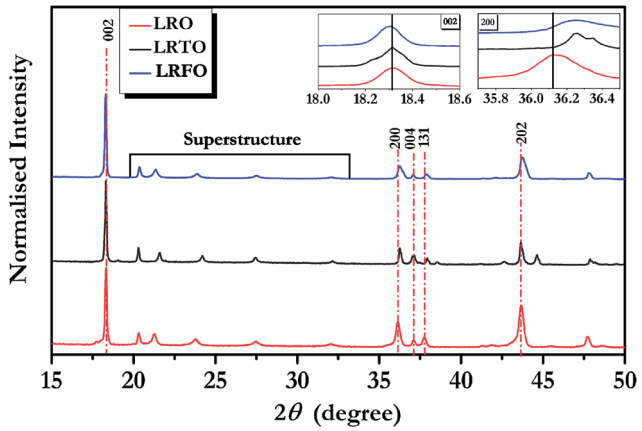

Fig. 2 Comparison of the diffraction patterns of LRO, LRTO and LRFO. Inset indicates nature of peak shift.

fit a rhombohedral space group. But on the inclusion of these peaks into the Rietveld refinement it is noted that the monoclinic $C2/c$ provides a better fit, this fact has been reported multiple times in literature.[45,50,51] The calculated lattice parameters are indicated in Table 2. The Rietveld refinement is indicated in Fig. S1, ESI.† The change in the lattice parameters can be explained as follows; the parent structure consists of alternating TM and lithium layers and the oxygen atoms are arranged in a cubic closed packing pattern. The TM layer consists of Li and Ru ions mixed in a 1 : 2 ratio. The layer is composed of six MO_6 octahedras arranged in a honeycomb pattern around Li atoms as indicated in Fig. 1. The Ru atoms in LRO are able to form quadruple bonds with neighbouring RuO_6 octahedras leading to the formation of highly ordered continuous hexagonal Ru networks in alternate basal planes. In the case of LRFO and LRTO one in every four Ru^{4+} sites is replaced by Fe and Ti respectively. These metals then form quadruple bonds with Ru but because of the smaller ionic radii of both Fe and Ti the bond lengths of these are different from that observed for LRO (Ru–Ru = 3.04(8) Å, Ru–Fe = 2.95(7) Å and Ru–Ti = 2.96(4) Å), resulting in distortion of the honeycomb structure. The smaller bond length ensures a higher stability of the TM layer.[26,52] Apart from the change in lattice parameters significant peak broadening is observed for 200 and 202 peaks in the case of LRFO, similar characteristics have been observed by McCalla *et al.*[37] for the presence of an extra Fe rich phase in Li–Fe–Te–O. Fig. S4† illustrates the results of EDX mapping of LRFO, a uniform distribution of Fe and Ru are found in the sample. Confirming no specific Fe rich zones. The peak broadening instead can be attributed to smaller crystallite size in the case of LRFO (Table S1†).

Table 2 Rietveld refined lattice parameters of LRO, LRTO and LRFO

Phase	LRO	LRTO	LRFO
Space group	$C2/c$	$C2/c$	$C2/c$
a (Å)	4.91(4)	5.03(1)	5.04(4)
b (Å)	8.76(1)	8.72(7)	8.75(6)
c (Å)	9.85(5)	9.84(8)	9.84(9)
β (°)	99.96(5)	99.79(7)	99.89(5)
R_{wp}	6.30	5.61	4.36

Fig. 3a–c illustrates the electron micrographs recorded for LRO, LRFO and LRTO. Cursory examination indicates that the particle size is almost double that of LRFO and LRTO. Smaller particle size can also lead to increase in total capacity of the materials because of a larger interaction area with the electrolyte. The precise reason for the smaller size of LRFO and LRTO is not known and is under investigation.

3.1 Electrochemical studies

Cyclic voltammetry (CV) curves for each of the samples was recorded at a slow rate of 0.1 mV s^{-1} and is illustrated in Fig. 4a–c. It is interesting to note that each of the materials has a slightly different charge transfer route, for example, in the case of LRO, the charge is mainly stored by the reversible oxidation of Ru (Ru^{4+}/Ru^{5+}). In LRTO, Ti merely acts as a supporting structure for the LiM_2 layer as the Ti redox couple is not active in the selected potential range (2–4.6 V *vs.* Li).[53,54] Whereas LRFO exhibits two redox reactions with varying degree of reversibility, the first being the (Ru^{4+}/Ru^{5+} at 3.75 V *vs.* Li) transition and second being the (Fe^{3+}/Fe^{4+} at 4 V *vs.* Li) redox couple.[55,56]

In the case of LRO and LRTO, as the cell is charged to 3.75 V *vs.* Li a redox peak corresponding to the oxidation of Ru can be

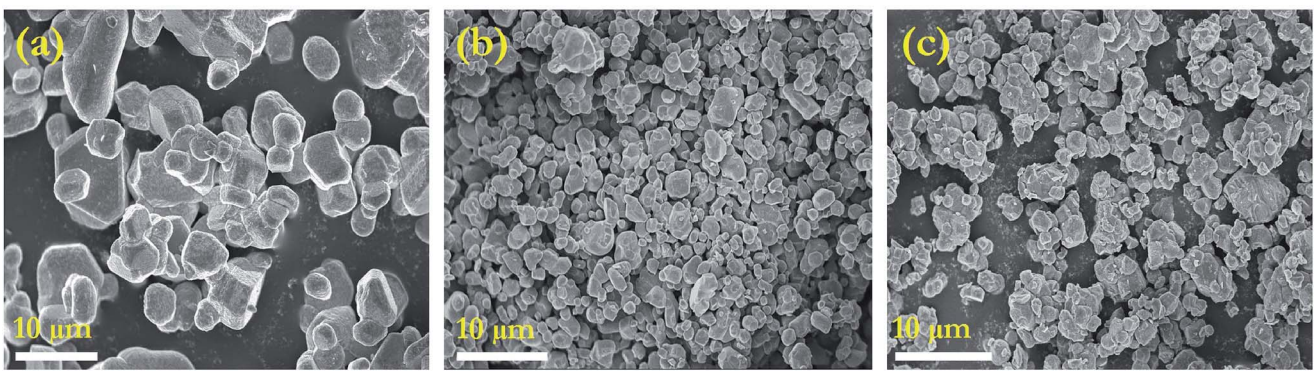

Fig. 3 SEM micrograph of (a) LRO, (b) LRTO and (c) LRFO.

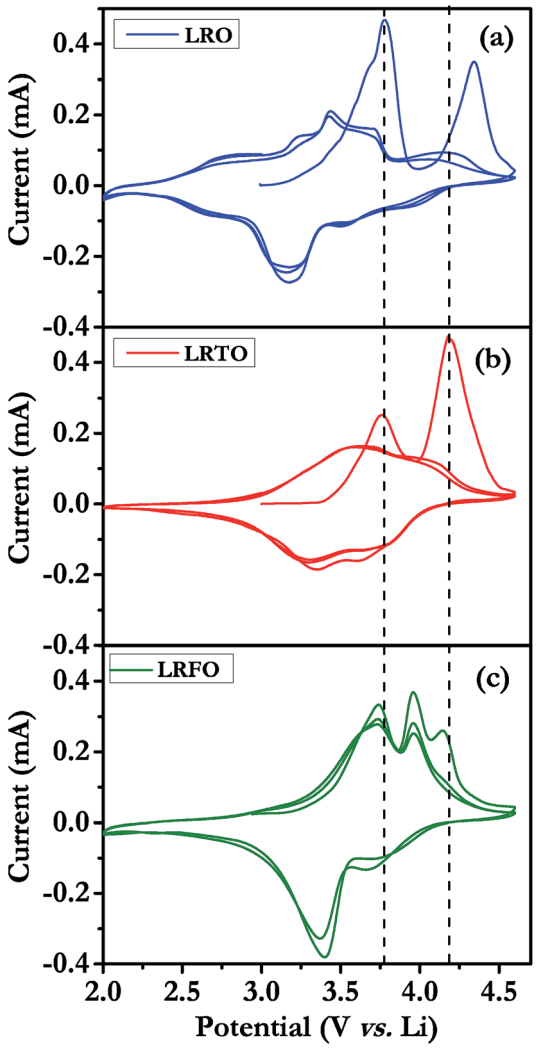

Fig. 4 CV trace recorded for the first two cycles at 0.1 mV s^{-1} between 2 and 4.6 V *vs.* Li (a) LRO, (b) LRTO and (c) LRFO.

observed. When charged up to 4.6 V *vs.* Li a sharp peak appears at ~4.4 V *vs.* Li for LRO and ~4.25 V *vs.* Li for LRTO. The physical implication can be argued to be either of the two following reactions.

- Oxygen gas is irreversibly removed from the surface.[57]
- Or following the argument by Sathiya *et al.*[23,24] the peak can indicate a reversible anionic redox reaction occurring at oxygen centres. During the second cycle the intensity of this peak is greatly diminished indicating that oxygen evolution is more likely.

During the cathodic scan, it can be noted that the peak corresponding to the oxygen anionic redox process ~4.25 V *vs.* Li is not observed. The reason for this is not understood to date. Apart from this it can be noted that the peak at ~3.25 V *vs.* Li corresponding to the reduction of Ru^{5+} is highly diminished in both cases (more obvious for LRTO) this can be attributed to structural rearrangement in both the samples after removal of O_2 during the charge process. Due to this a significant loss in long range order can be expected.[24]

In stark contrast, the CV profile of the LRFO exhibits three sharp peaks. The peak at ~3.75 V *vs.* Li corresponds to the oxidation of Ru from a +4 state to a +5 state. The peak at ~4.0 V *vs.* Li from previous literature can be attributed to a combination of the oxidation of $Fe^{3+} \rightarrow Fe^{4+}$ and for the creation of O_2^{n-} type species. The third peak at ~4.2 V *vs.* Li corresponds irreversible removal of oxygen from the molecule. At this stage it is important to point out that the substitution of Ru with Fe has resulted in a number of positive effects.

- It has significantly reduced the irreversible capacity lost due to oxygen evolution (purely based on the current observed in the CV profile) by triggering the formation of O_2^{n-} type species.[28,36]
- Based on the highly symmetric nature of the CV profile even after the first cycle it can be safely assumed that the material predominantly retains its original crystal structure.[58–60]

Fig. 5a illustrates the charge–discharge curves for LRO, LRFO and LRTO (tested at C/5 between 2 and 4.6 V *vs.* Li), it is noted that LRFO is able to generate a discharge capacity of ~250 mA h g^{-1} whilst LRTO and LRO deliver a capacity of ~230 mA h g^{-1} and ~210 mA h g^{-1} respectively. Indicating that the partial substitution of Ru with Fe leads to an increase in discharge capacity when compared to Ti substitution. To confirm that the increase in capacity is not due to just a reduction in molecular weight charge discharge curves w.r.t to number of Li atoms reversibly extracted is plotted in Fig. S5.† Fig. 5b illustrates the capacity retention behaviour of each of the LLCs and it can be

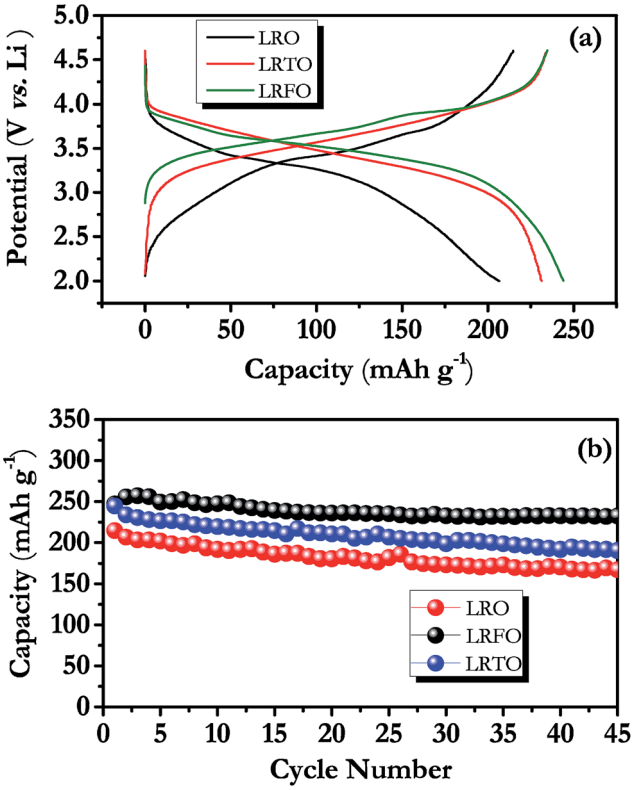

Fig. 5 (a) Galvanostatic charge discharge profile of LRO, LRTO and LRFO; (b) cycle number *vs.* capacity for LRO, LRFO and LRTO for the first 45 cycles.

observed that LRFO is able to maintain 93% of its initial capacity after 45 cycles but in the case of LRO and LRTO only 78 and 77% respectively was retained. This increase in capacity and cycle life warrants a further in-depth study on the charge storage mechanism of LRFO. The excess capacity observed can be attributed to the removal of ~1.6 moles of Li from the host structure. The oxidation and reduction process occurring in the TM atoms accounts for only 1 mole of Li. The extra Li can be understood to be stored by the means of an anionic redox reaction occurring at the oxygen centres. The mechanism and conditions required for such a reaction has been studied by various groups.[23,24,28,61] But to the best of our knowledge this is the first report on a Ru–Fe based system in which the inclusion of Fe in such a system indicates an immense improvement in cycle stability (up to 93% retention in the first 45 cycles) wherein previous reports on Fe based systems exhibited 40% loss in capacity within the first two cycles.[36] In our opinion this is mainly achieved by significantly reducing the oxygen evolution reaction by triggering a stable anionic redox reaction instead. The structural changes leading to such an improvement in capacity retention are studied in the following sections.

3.2 *In situ* X-ray diffraction studies

In order to understand the nature of structural changes in the bulk of LRFO, *in operando* X-ray diffraction was employed. Fig. 6 correlates the first cycle with the *in operando* X-ray diffraction pattern collected. The pristine pattern has an O3 type layered structure. As the material is charged up to a potential of ~3.25 V *vs.* Li, low intensity shoulder peaks are observed on the left of (200), (202) and (204) peaks, simultaneously there is a gradual reduction in the area of the (004) and (131) peaks. Between 3.25 V and 3.6 V *vs.* Li, the shoulder peaks experience an increase in intensity while the (004) and (131) peaks coalesce to form a single reflection. Once the cell is completely charged up to 4.6 V *vs.* Li the new rhombohedral de-lithiated phase completely replaces the pristine monoclinic phase. The reason for the formation of this phase is not completely understood, but two possible explanations can be, Jahn–Teller distortion due to high spin Fe(IV)[62] or structural compensations due to removal of Li from the structure.[63] To understand this phenomena completely *in operando* X-ray absorption studies are carried out on the Fe K-edge and the Ru K-edge.

3.3 *In operando* X-ray absorption studies

Modified CR2016 type coin cells with 3 mm central holes were used to measure the XAS spectra of the Ru and Fe K edge. The Ru K-edge was studied as the sample is charged and discharged. The spectra was matched with sample spectra of RuO_2 (ESI Fig. S3†) and it was confirmed that Ru in LRFO exists in a +4 oxidation state. Fig. 7 illustrates the change in the spectra as the sample is charged. It can be noted that the absorption edge gradually shifts ~2 eV towards a higher energy up to ~3.75 V *vs.* Li indicating that the oxidation of Ru is complete at this time. No further shift is observed till 4.6 V *vs.* Li. During the discharge, the shift in the edge proceeds with a reverse trend. At the end of discharge, Ru returns back to its +4 state. The Fe K-

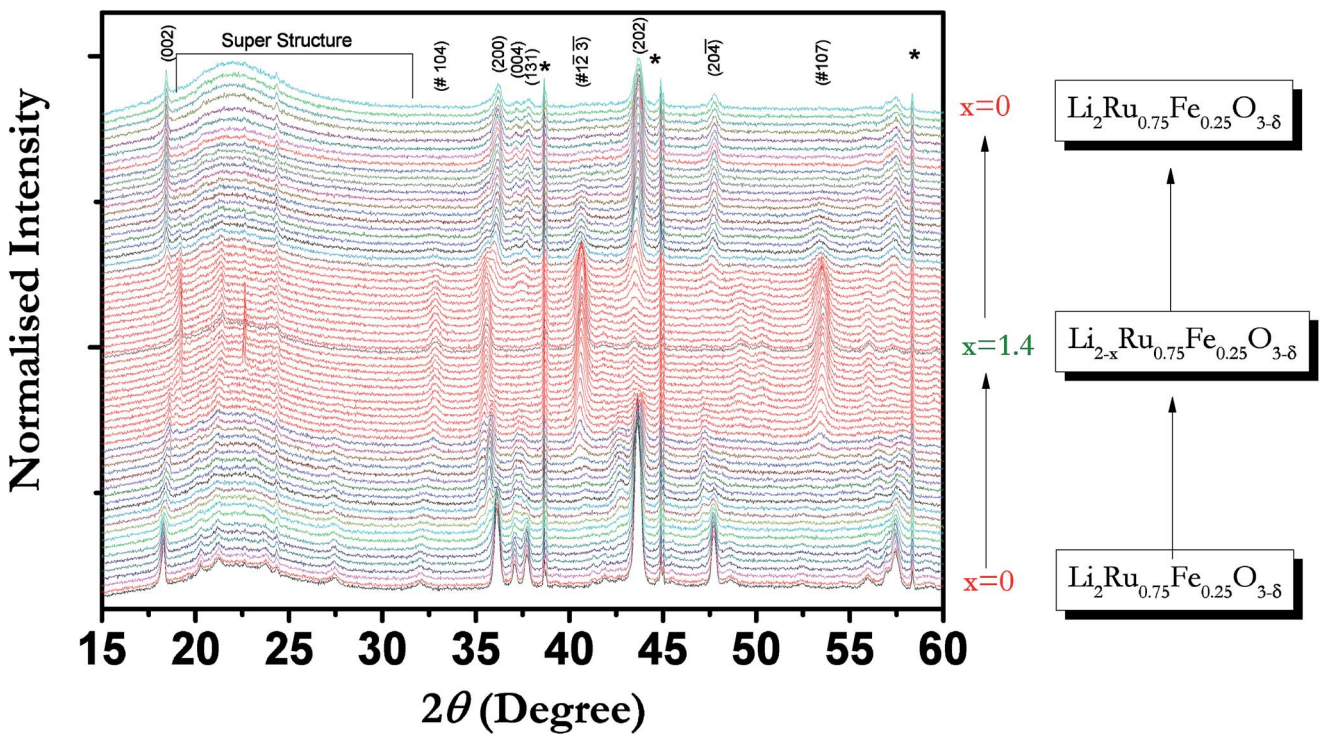

Fig. 6 *In operando* XRD pattern of LRFO corresponding to 1 charge discharge cycle. The region highlighted in red indicates the formation of the de-lithiated rhombohedral phase. Reflections pertaining to this phase have been prefixed with a "#". Peaks occurring because of the presence of the aluminium cover on the electrochemical cell are indicated with a "*". The value of '*x*' is calculated using the final capacity recorded.

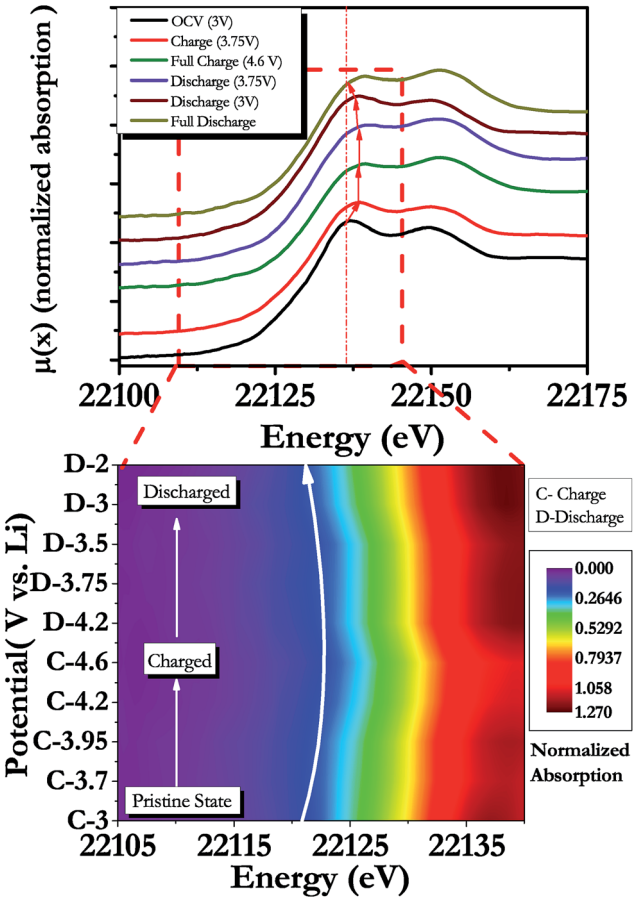

Fig. 7 XANES spectra of ruthenium during one full charge and discharge, zoomed in portion better represents the movement of the Ru K-edge during cycling.

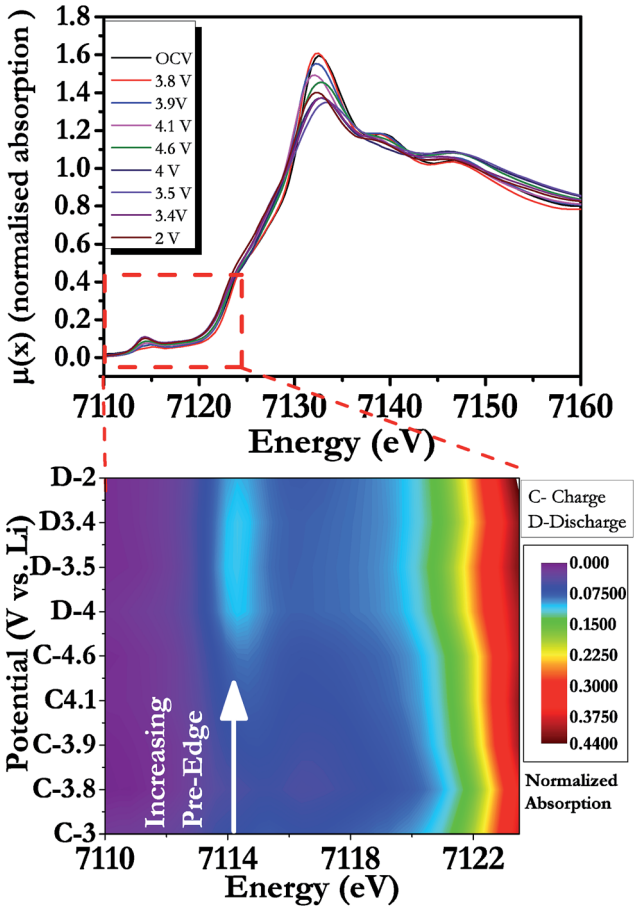

Fig. 8 XANES spectra of iron during one full charge and discharge, inset: variation of the pre-edge during cycling.

edge was studied in a similar manner. The pristine spectra was matched with pure powder sample of Fe (ESI Fig. S3†) and from that, we were able to establish that Fe initially is present in a +3 oxidation state. But contrary to our expectation no change in the absorption edge was observed during cycling (Fig. 8) similar behaviour has been noted in the case of Li–Fe–Te oxides wherein both the Fe and Te do not change their respective oxidation states during cycling but DFT studies indicate massive changes in the co-ordination environment of Fe[37] which gradually leads to material degradation. In the case of LRFO the change in the Fe co-ordination environment is probed directly by observing the nature of change in the pre-edge during cycling. The pre-edge corresponds to the 1s → 3d transition region,[64] and is very sensitive to parameters such as centro-symmetry, geometry, oxidation state, spin state.[65,66] For complexes in a centro-symmetric arrangement such as Fe or Ru in octahedral arrangement a dipole coupled 1s → 3d transition is forbidden in order to maintain parity.[66,67] Experimentally, in case of a centro-symmetric structure the 1s → 3d transitions are considered to be extremely weak and occur mainly due to direct quadruple coupling. Any deviation from centro-symmetry allows the mixing of the dipole and quadruple 1s → 3d transitions. Earlier studies have established that the electric quadrupole is approximately two orders of magnitude weaker than the electric dipole coupling.[68,69] Thus, making the intensity of the pre-edge highly sensitive to the coordination environment of the element being studied.

The spectra recorded at OCV conditions (Fig. 8) displays no deformations in the pre-edge implying Fe is located in a centro-symmetric environment. Further charging leads to an increase in intensity of the pre-edge. This can be explained by a loss of symmetry in the complex leading to the mixing of metal 4p with 3d orbitals which provides a certain dipole allowed 1s → 4d character to the transition.[65] The appearance of the pre-edge feature provides conclusive evidence for the distortion of the Fe octahedra during the charge process.[70–73] As the cell is discharged it can be expected that the pre-edge returns to its original value but no such effect is observed indicating that the Fe coordination environment is permanently distorted. A possible explanation is:

• At 4 V the second lithium atom begins to be removed from the host structure this is compensated by the oxidation of Fe(III) to Fe(IV). As all the Fe in the structure is oxidised, any further charging triggers the formation of $2O^{-}$ type species, resulting in the reorganisation of oxygen network in the material leading to distortion of the TM layer.[28]

• The formation of these O–O dimers leads to a O → TM electron transfer, this is called reductive coupling. Oxygen vacancies have been known to be difficult to create in pure 4d TMs(Ru) but a mixing of Ru and Fe is favourable to improve the structural stability and prevent the complete loss of lattice oxygen during the charge process.[74]

The Fourier transform of the extended X-ray absorption fine structure (EXAFS) spectra of the Fe K-edge is investigated to get a better idea about the nature of the reaction at the Fe centre during electrochemical cycling. For this purpose, we only focus on the first Fe–O shell (details of the fitting are included in the ESI Table S1, Fig. S2†). It can be noted that during the charge portion up to 3.75 V there is little change in the Fe–O distance, but on increasing the potential Fe is oxidized to Fe^{4+} leading to reduction in the Fe–O distance (ESI Table S1†). During the discharge phase, it is expected that the Fe–O distance should recover completely but such behaviour is not observed (at 3.7 V *vs.* Li, a decrease in radial distance is observed which could be caused by reduction of Ru in the cell leading to rearrangement of the oxygen atoms). This supports our argument that Fe–O coordination environment undergoes a permanent distortion. The exact nature of the changes in the oxygen network and the formation of the peroxo species is further observed using O K-edge XAS.

3.4 Oxygen X-ray absorption spectroscopy

O K-edge XAS was collected for the LRFO electrodes, the results for which have been elucidated in Fig. 9. It can be noted that all of the patterns can be broadly divided into two parts. The lower energy features (<535 eV) can be attributed to the oxygen 2p weight in orbitals with dominant transition metal character (the metal 3d band). The second region 5–10 eV above the threshold is attributed to the oxygen p character hybridised with the metal 4s and 4p states. The large energy spread of the O 1s spectra is expected because of the highly covalent nature of these compounds.[75]

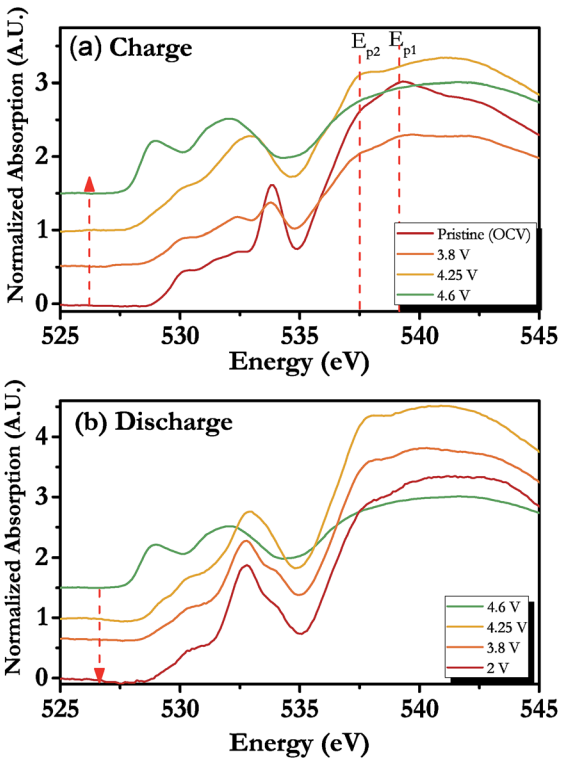

Fig. 9 O 1s spectra collected at specific points during the (a) charge and (b) discharge process.

The 4sp bands can be split into two portions the E_{p1} and E_{p2}, which is the low energy shoulder peak observed while charging the cell. This structure has been previously related to the presence of oxygen in an octahedral arrangement and has been shown to have no strong dependence on the crystal structure of the system.[75] It can be noted that up to 4.25 V, the oxygen atoms retain an octahedral environment. At full charge (4.6 V *vs.* Li), E_{p1} and E_{p2} combine into a single peak which can be interpreted as the transition of an electron to a σ* state.[76] The observed shift to higher energy orbital indicates a shortening of the M–O bond, leading to deformation of the perfect octahedra, which is in direct correlation with our observations regarding the Fe and Ru K edge.[75–77]

During the discharge cycle, it can be noted that the O_H arrangement around the oxygen atoms is partially regained (Fig. 9b).[75] This behaviour indicates that the reaction occurring at the oxygen centre is reversible to a certain extent and is the reason for the additional charge storage ability of lithium rich layered materials.

Investigation between 520 and 535 eV probes the interaction between oxygen and metal hybridized states. Four distinct peaks corresponding to Ru and Fe (t_{2g} and e_g) can be observed at OCV. The intensity of these peaks can be explained by a variety of factors such as covalency, ligand effects[76] *etc.* For the purpose of this study, we predominantly concentrate on the occurrence of the peak at 533 eV during charge at 4.25 V *vs.* Li. This peak is attributed to the formation of peroxo/superoxo type linkages between oxygen atoms.[78] The hole formed in this manner is the stabilised on the anti-bonding σ* orbital of the O–O bond.[78] Further discharge leads to the formation of a different set of peaks which cannot be matched with the peaks observed in the charge cycle. The nature of the reaction is not well understood at this stage and further experiments are needed to explain these results clearly.

4 Conclusion

During the course of this study, effect of partial substitution of Ru with Fe was compared to LRO and LRTO. LRO, LRTO and LRFO were all synthesised using a solid state route. Rietveld refinement of the samples indicates that the desired layered structure was formed. On electrochemically testing each of the samples it was noted that Fe substituted samples not only displayed a higher capacity but also a higher degree of reversibility, coupled with a higher insertion voltage, which provides a considerable advantage in terms of its application in high energy density batteries.

In operando X-ray diffraction techniques were used to establish that a phase change from a lithiated monoclinic to

a partially delithiated rhombohedral takes place during the cycling process. Such phase change can possibly manipulate frontier orbitals leading to the activation of an anionic redox reaction. *In operando* X-ray absorption techniques were employed to study the nature of change occurring at Ru and Fe center. It was concluded that Ru atoms undergo a Ru(IV) → Ru(V) redox reaction during the charge–discharge reaction. But, Fe atoms are in stark contrast as no change in the absorption edge could be observed during the cycling. Instead an irreversible change in the pre-edge was observed indicating a distortion of Fe–O octahedra during cycling which was confirmed by analyzing FT of the EXAFS spectra. Further, studies were conducted at oxygen centers using soft X-rays, this experiment for the first time could impart direct evidence of the formation of the peroxo/superoxo type linkages during cycling. The high energy range of the O K-edge spectra confirmed that oxygen atoms were undergoing a reversible change in their coordination environment during cycling.

The results of this study clearly indicate that partial substitution of Ru with Fe leads to a phase change during cycling facilitating the activation of an anionic redox reaction. The involvement of the anionic redox reaction leads to an increase in the discharge capacity of the material. The introduction of iron also leads to an increase in the cycling ability and reduction of voltage decay when compared to previous results such as those published by Saubanere *et al.* However certain issues observed during the testing could not be addressed in this manuscript such as the nature of the reaction between Fe^{4+} and O_2^{n-} species and how this influences the charge storage in the cell when compared to other d^0 or d^{10} type substitutions previously studied in literature.[26] Further studies relating to first principle calculations on the nature of the reaction are under progress.

Acknowledgements

We would like to acknowledge the contributions of the staff from SSRL, Stanford University for their guidance and technical support for the measurement of the Fe, Ru and O absorption edges. Use of the Stanford Synchrotron Radiation Lightsource, SLAC National Accelerator Laboratory, is supported but the U.S. Department of Energy, Office of Science, Office of Basic Energy Sciences under Contract No. DE-AC02-76F00515. The 'Kwanjeong Education Foundation Fellowship' for their financial support of Kipil Lim during his PhD. This work was financially supported by Ministry of Education (MOE TIER 2 funding MOE2015-T2-1-046), Singapore.

References

1 K. Ozawa, *Solid State Ionics*, 1994, **69**, 212–221.
2 J. M. Tarascon, E. Wang, F. Shokoohi, W. McKinnon and S. Colson, *J. Electrochem. Soc.*, 1991, **138**, 2859–2864.
3 H. Huang and P. G. Bruce, *J. Electrochem. Soc.*, 1994, **141**, L106–L107.
4 A. K. Padhi, K. Nanjundaswamy and J. Goodenough, *J. Electrochem. Soc.*, 1997, **144**, 1188–1194.
5 R. A. Leising, M. J. Palazzo, E. S. Takeuchi and K. J. Takeuchi, *J. Electrochem. Soc.*, 2001, **148**, A838–A844.
6 M. S. Whittingham, *Chem. Rev.*, 2014, **114**, 11414–11443.
7 M. Thackeray, *J. Electrochem. Soc.*, 1995, **142**, 2558–2563.
8 T. J. Boyle, D. Ingersoll, T. M. Alam, C. J. Tafoya, M. A. Rodriguez, K. Vanheusden and D. H. Doughty, *Chem. Mater.*, 1998, **10**, 2270–2276.
9 M. S. Whittingham, *Chem. Rev.*, 2004, **104**, 4271–4302.
10 J. Choi and A. Manthiram, *J. Electrochem. Soc.*, 2005, **152**, A1714–A1718.
11 H. Yoshizawa and T. Ohzuku, *J. Power Sources*, 2007, **174**, 813–817.
12 F. Yang, Y. Liu, S. K. Martha, Z. Wu, J. C. Andrews, G. E. Ice, P. Pianetta and J. Nanda, *Nano Lett.*, 2014, **14**, 4334–4341.
13 D. Mohanty, S. Kalnaus, R. A. Meisner, K. J. Rhodes, J. Li, E. A. Payzant, D. L. Wood and C. Daniel, *J. Power Sources*, 2013, **229**, 239–248.
14 S. Hy, F. Felix, J. Rick, W.-N. Su and B. J. Hwang, *J. Am. Chem. Soc.*, 2014, **136**, 999–1007.
15 J. Zheng, P. Xu, M. Gu, J. Xiao, N. D. Browning, P. Yan, C. Wang and J.-G. Zhang, *Chem. Mater.*, 2015, **27**, 1381–1390.
16 C. S. Yoon, M. H. Choi, B.-B. Lim, E.-J. Lee and Y.-K. Sun, *J. Electrochem. Soc.*, 2015, **162**, A2483–A2489.
17 A. Manthiram, J. C. Knight, S.-T. Myung, S.-M. Oh and Y.-K. Sun, *Adv. Energy Mater.*, 2016, **6**, 1501010.
18 Y.-K. Sun and S.-H. Jin, *J. Mater. Chem.*, 1998, **8**, 2399–2404.
19 B. Scrosati and J. Garche, *J. Power Sources*, 2010, **195**, 2419–2430.
20 J. W. Fergus, *J. Power Sources*, 2010, **195**, 939–954.
21 C. Chen, J. Liu, M. Stoll, G. Henriksen, D. Vissers and K. Amine, *J. Power Sources*, 2004, **128**, 278–285.
22 P. Rozier and J. M. Tarascon, *J. Electrochem. Soc.*, 2015, **162**, A2490–A2499.
23 M. Sathiya, G. Rousse, K. Ramesha, C. P. Laisa, H. Vezin, M. T. Sougrati, M. L. Doublet, D. Foix, D. Gonbeau, W. Walker, A. S. Prakash, M. Ben Hassine, L. Dupont and J. M. Tarascon, *Nat. Mater.*, 2013, **12**, 827–835.
24 M. Sathiya, A. M. Abakumov, D. Foix, G. Rousse, K. Ramesha, M. Saubanère, M. L. Doublet, H. Vezin, C. P. Laisa, A. S. Prakash, D. Gonbeau, G. VanTendeloo and J. M. Tarascon, *Nat. Mater.*, 2015, **14**, 230–238.
25 M. Sathiya, K. Ramesha, G. Rousse, D. Foix, D. Gonbeau, A. Prakash, M. Doublet, K. Hemalatha and J.-M. Tarascon, *Chem. Mater.*, 2013, **25**, 1121–1131.
26 A. K. Kalathil, P. Arunkumar, D. H. Kim, J.-W. Lee and W. B. Im, *ACS Appl. Mater. Interfaces*, 2015, **7**, 7118–7128.
27 A. Grimaud, W. Hong, Y. Shao-Horn and J.-M. Tarascon, *Nat. Mater.*, 2016, **15**, 121–126.
28 M. Saubanère, E. McCalla, J.-M. Tarascon and M.-L. Doublet, *Energy Environ. Sci.*, 2016, **9**, 984–991.
29 J. Rouxel, *Physica B+C*, 1980, **99**, 3–11.
30 J. Rouxel, *Chem.–Eur. J.*, 1996, **2**, 1053–1059.
31 J. Tarascon, G. Vaughan, Y. Chabre, L. Seguin, M. Anne, P. Strobel and G. Amatucci, *J. Solid State Chem.*, 1999, **147**, 410–420.

32 F. Gillot, S. Boyanov, L. Dupont, M.-L. Doublet, M. Morcrette, L. Monconduit and J.-M. Tarascon, *Chem. Mater.*, 2005, **17**, 6327–6337.
33 S. Boyanov, K. Annou, C. Villevieille, M. Pelosi, D. Zitoun and L. Monconduit, *Ionics*, 2008, **14**, 183–190.
34 A. K. Padhi, K. S. Nanjundaswamy, C. Masquelier, S. Okada and J. B. Goodenough, *J. Electrochem. Soc.*, 1997, **144**, 1609–1613.
35 M. Sathiya, K. Ramesha, G. Rousse, D. Foix, D. Gonbeau, K. Guruprakash, A. Prakash, M. Doublet and J.-M. Tarascon, *Chem. Commun.*, 2013, **49**, 11376–11378.
36 E. McCalla, M. T. Sougrati, G. Rousse, E. J. Berg, A. Abakumov, N. Recham, K. Ramesha, M. Sathiya, R. Dominko, G. Van Tendeloo, *et al.*, *J. Am. Chem. Soc.*, 2015, **137**, 4804–4814.
37 E. McCalla, A. S. Prakash, E. Berg, M. Saubanère, A. M. Abakumov, D. Foix, B. Klobes, M.-T. Sougrati, G. Rousse, F. Lepoivre, *et al.*, *J. Electrochem. Soc.*, 2015, **162**, A1341–A1351.
38 S. Hartung, N. Bucher, R. Bucher and M. Srinivasan, *Rev. Sci. Instrum.*, 2015, **86**, 086102.
39 B. Ravel and M. Newville, *J. Synchrotron Radiat.*, 2005, **12**, 537–541.
40 K. G. Tirsell and V. P. Karpenko, *Nucl. Instrum. Methods Phys. Res., Sect. A*, 1990, **291**, 511–517.
41 J. Hong, H. Gwon, S.-K. Jung, K. Ku and K. Kang, *J. Electrochem. Soc.*, 2015, **162**, A2447–A2467.
42 A. C. W. P. James and J. B. Goodenough, *J. Solid State Chem.*, 1988, **74**, 287–294.
43 K. Kataoka, Y. Takahashi, N. Kijima, H. Nagai, J. Akimoto, Y. Idemoto and K.-i. Ohshima, *Mater. Res. Bull.*, 2009, **44**, 168–172.
44 G. Dittrich and R. Hoppe, *Z. Anorg. Allg. Chem.*, 1969, **371**, 306–317.
45 K. A. Jarvis, Z. Deng, L. F. Allard, A. Manthiram and P. J. Ferreira, *Chem. Mater.*, 2011, **23**, 3614–3621.
46 N. V. Tarakina, T. Denisova, L. Maksimova, Y. Baklanova, A. Tyutyunnik, I. Berger, V. Zubkov and G. Van Tendeloo, *Z. Kristallogr.*, 2009, **36**, 37.
47 H. Kobayashi, M. Tabuchi, M. Shikano, H. Kageyama and R. Kanno, *J. Mater. Chem.*, 2003, **13**, 957–962.
48 N. V. Tarakina, T. Denisova, L. Maksimova, Y. Baklanova, A. Tyutyunnik, I. Berger, V. Zubkov and G. Van Tendeloo, *Z. Kristallogr.*, 2009, **36**, 37.
49 J. Ma, Y.-N. Zhou, Y. Gao, X. Yu, Q. Kong, L. Gu, Z. Wang, X.-Q. Yang and L. Chen, *Chem. Mater.*, 2014, **26**, 3256–3262.
50 M. Thackeray, S.-H. Kang, C. Johnson, J. Vaughey and S. Hackney, *Electrochem. Commun.*, 2006, **8**, 1531–1538.
51 C. Johnson, S. Korte, J. Vaughey, M. Thackeray, T. Bofinger, Y. Shao-Horn and S. Hackney, *J. Power Sources*, 1999, **81**, 491–495.
52 T. Ungár, *Scr. Mater.*, 2004, **51**, 777–781.
53 H.-G. Jung, J. Kim, B. Scrosati and Y.-K. Sun, *J. Power Sources*, 2011, **196**, 7763–7766.
54 Z. Yang, D. Choi, S. Kerisit, K. M. Rosso, D. Wang, J. Zhang, G. Graff and J. Liu, *J. Power Sources*, 2009, **192**, 588–598.
55 E. Lee, D. E. Brown, E. E. Alp, Y. Ren, J. Lu, J.-J. Woo and C. S. Johnson, *Chem. Mater.*, 2015, **27**, 6755–6764.
56 M. Holzapfel, O. Proux, P. Strobel, C. Darie, M. Borowski and M. Morcrette, *J. Mater. Chem.*, 2004, **14**, 102–110.
57 Z. Deng and A. Manthiram, *J. Phys. Chem. C*, 2011, **115**, 7097–7103.
58 E. Uchaker, Y. Zheng, S. Li, S. Candelaria, S. Hu and G. Cao, *J. Mater. Chem. A*, 2014, **2**, 18208–18214.
59 A. L. Viet, M. Reddy, R. Jose, B. Chowdari and S. Ramakrishna, *J. Phys. Chem. C*, 2009, **114**, 664–671.
60 J. Qi, P. Xu, Z. Lv, X. Liu and A. Wen, *J. Alloys Compd.*, 2008, **462**, 164–169.
61 E. McCalla, A. M. Abakumov, M. Saubanère, D. Foix, E. J. Berg, G. Rousse, M.-L. Doublet, D. Gonbeau, P. Novák, G. Van Tendeloo, *et al.*, *Science*, 2015, **350**, 1516–1521.
62 M. Vračar, A. Kuzmin, R. Merkle, J. Purans, E. A. Kotomin, J. Maier and O. Mathon, *Phys. Rev. B: Condens. Matter Mater. Phys.*, 2007, **76**, 174107.
63 S. Okada, Y. Takahashi, T. Kiyabu, T. Doi, J.-I. Yamaki and T. Nishida, *Meet. Abstr.*, 2006, 201.
64 J. E. Hahn, R. A. Scott, K. O. Hodgson, S. Doniach, S. R. Desjardins and E. I. Solomon, *Chem. Phys. Lett.*, 1982, **88**, 595–598.
65 T. E. Westre, P. Kennepohl, J. G. DeWitt, B. Hedman, K. O. Hodgson and E. I. Solomon, *J. Am. Chem. Soc.*, 1997, **119**, 6297–6314.
66 G. Shulman, Y. Yafet, P. Eisenberger and W. Blumberg, *Proc. Natl. Acad. Sci. U. S. A.*, 1976, **73**, 1384–1388.
67 L. Huff and W. Houston, *Phys. Rev.*, 1930, **36**, 842.
68 R. A. Bair and W. A. Goddard III, *Phys. Rev. B: Condens. Matter Mater. Phys.*, 1980, **22**, 2767.
69 C. Brouder, *J. Phys.: Condens. Matter*, 1990, **2**, 701.
70 M. Wilke, F. Farges, P.-E. Petit, G. E. Brown and F. Martin, *Am. Mineral.*, 2001, **86**, 714–730.
71 R. Sarangi, N. Aboelella, K. Fujisawa, W. B. Tolman, B. Hedman, K. O. Hodgson and E. I. Solomon, *J. Am. Chem. Soc.*, 2006, **128**, 8286–8296.
72 G. Shulman, Y. Yafet, P. Eisenberger and W. Blumberg, *Proc. Natl. Acad. Sci. U. S. A.*, 1976, **73**, 1384–1388.
73 T. E. Westre, P. Kennepohl, J. G. DeWitt, B. Hedman, K. O. Hodgson and E. I. Solomon, *J. Am. Chem. Soc.*, 1997, **119**, 6297–6314.
74 Y. Xie, M. Saubanère and M.-L. Doublet, *Energy Environ. Sci.*, 2017, **10**(1), 266–274.
75 F. De Groot, M. Grioni, J. Fuggle, J. Ghijsen, G. Sawatzky and H. Petersen, *Phys. Rev. B: Condens. Matter Mater. Phys.*, 1989, **40**, 5715.
76 F. De Groot and A. Kotani, *Core level spectroscopy of solids*, CRC press, 2008.
77 F. De Groot, G. Vankó and P. Glatzel, *J. Phys.: Condens. Matter*, 2009, **21**, 104207.
78 B. Mortemard de Boisse, G. Liu, J. Ma, S.-i. Nishimura, S.-C. Chung, H. Kiuchi, Y. Harada, J. Kikkawa, Y. Kobayashi, M. Okubo and A. Yamada, *Nat. Commun.*, 2016, **7**, 11397.

